

Microvasculature alters the dispersion properties of shear waves – a multi-frequency MR elastography study

Lauriane Jugé^{a,b}, Anne Petiet^d, Simon A. Lambert^e, Pascal Nicole^f, Simon Chatelin^g, Valerie Vilgrain^{g,h}, Bernard E. Van Beers^{g,h}, Lynne E. Bilston^{a,c} and Ralph Sinkus^{e*}

Magnetic Resonance Elastography (MRE) uses macroscopic shear wave propagation to quantify mechanical properties of soft tissues. Micro-obstacles are capable of affecting the macroscopic dispersion properties of shear waves. Since disease or therapy can change the mechanical integrity and organization of vascular structures, MRE should be able to sense these changes if blood vessels represent a source for wave scattering. To verify this, MRE was performed to quantify alteration of the shear wave speed c_s due to the presence of vascular outgrowths using an aortic ring model. Eighteen fragments of rat aorta included in a Matrigel matrix ($n=6$ without outgrowths, $n=6$ with a radial outgrowth extent of $\sim 600\mu\text{m}$ and $n=6$ with $\sim 850\mu\text{m}$) were imaged using a 7 Tesla MR scanner (Bruker, PharmaScan). High resolution anatomical images were acquired in addition to multi-frequency MRE ($\nu = 100, 115, 125, 135$ and 150 Hz). Average c_s was measured within a ring of $\sim 900\mu\text{m}$ thickness encompassing the aorta and were normalized to c_{s0} of the corresponding Matrigel. The frequency dependence was fit to the power law model $c_s \sim \nu^y$. After scanning, optical microscopy was performed to visualize outgrowths. Results demonstrated that in presence of vascular outgrowths (1) normalized c_s significantly increased for the three highest frequencies (Kruskal-Wallis test, $P = 0.0002$ at 125 Hz and $P = 0.002$ at 135 Hz and $P = 0.003$ at 150 Hz) but not for the two lowest (Kruskal-Wallis test, $P = 0.63$ at 100 Hz and $P = 0.87$ at 115 Hz), and (2) normalized c_s followed a power law behavior not seen in absence of vascular outgrowths (ANOVA test, $P < 0.0001$). These results showed that vascular outgrowths acted as micro-obstacles altering the dispersion relationships of propagating shear waves and that MRE could provide valuable information about microvascular changes. Copyright © 2015 John Wiley & Sons, Ltd.

Keywords: MR elastography (MRE); viscoelasticity; aortic ring model; shear wave speed (c_s); structural imaging biomarkers

INTRODUCTION

Cancer growth is driven in part by abnormal angiogenesis that can be targeted by drug therapies. To date, anti-angiogenic agents have been indicated for tumor treatment, but no reliable non-invasive techniques have been identified that are capable

of differentiating responders from non-responders. At present, contrast-enhanced MRI (1–3) is routinely used clinically to monitor the tumor response to anti-angiogenic molecules. Radiological criteria, such as the Response Evaluation Criteria in Solid Tumors

* Correspondence to: R. Sinkus, King's College London, BHF Centre of Excellence, Division of Imaging Sciences and Biomedical Engineering, St. Thomas' Hospital, London SE1 7EH, United Kingdom.
E-mail: ralph.sinkus@kcl.ac.uk

a L. Jugé, L. E. Bilston
Neuroscience Research Australia, Randwick, Sydney, NSW, Australia

b L. Jugé
School of Medical Sciences, University of New South Wales, Kensington, Sydney, NSW, Australia

c L. E. Bilston
Prince of Wales Clinical School, University of New South Wales, Kensington, Sydney, NSW, Australia

d A. Petiet
Fédération de Recherche en Imagerie multimodalité (FRIM), U1148 INSERM, UFR de Médecine, University Paris Diderot, Sorbonne Paris Cité, Paris, France

e S. A. Lambert, R. Sinkus
King's College London, BHF Centre of Excellence, Division of Imaging Sciences and Biomedical Engineering, London, UK

f P. Nicole
Laboratory from inflammation to cancer in digestive diseases, UMR1149 INSERM, University Paris Diderot, Sorbonne Paris Cité, Paris, France

g S. Chatelin, V. Vilgrain, B. E. Van Beers
Laboratory of Imaging Biomarkers, UMR1149 INSERM, University Paris Diderot, Sorbonne Paris Cité, Paris, France

h V. Vilgrain, B. E. Van Beers
Department of Radiology, Beaujon University Hospital Paris Nord, Assistance Publique Hopitaux de Paris, APHP, Clichy, France

Abbreviations used: acqt/dir, acquisition time per direction; ANOVA, analysis of variance; c_s , shear wave speed; EASL, European Association for the Study of the Liver; FBS, fetal bovine serum; FOV, field of view; MRE, MR elastography; mRECIST, modified RECIST; RARE, rapid acquisition with refocused echoes; RECIST, Response Evaluation Criteria in Solid Tumors; ROI, region of interest; 2D/3D, two/three dimensional; ν , frequency; \varnothing , diameter.

1.1 (RECIST 1.1) (4) or, more recently, criteria which aim to analyze alterations in the perfused area, such as those of the European Association for the Study of the Liver (EASL) (5) and modified RECIST (mRECIST) (6), have been applied to evaluate the tumor response in hepatocellular carcinoma (7,8). These criteria assist clinicians to decide between the continuation or cessation of anti-angiogenic treatment. Although these criteria are sensitive to treatment-induced tumor necrosis, there is a poor correlation between the extent of tumor necrosis induced by new anti-angiogenic therapies and conventional methods of response assessment (8).

Anti-angiogenic treatment normalizes the vasculature supplying the tumor (9). This normalization changes the architecture of the affected vasculature. The presence or absence of these architectural changes is an indicator of the success or failure of therapy. A non-invasive imaging method which could provide an objective measurement and evaluation of the tissue's vasculature could represent a significant advance in the management of patients treated with targeted therapies.

Mechanical properties assessed at the millimeter scale have the potential to become a biomarker for microstructural changes in tissues, as they represent the integral sum of every individual microscopic component (10). Alterations in the mechanical integrity of these subcomponents, by disease or therapy, are likely to affect the apparent macroscopic mechanical properties of tissue, whereby micro-changes are reflected at the macroscopic scale. For example, the mechanical properties of hepatocytes, vascular structures and extracellular matrix all contribute to the biomechanical characteristics of liver parenchyma. Hepatocellular carcinoma has a denser cellularity, an increased amount of extracellular matrix and hypervascularization in comparison with healthy parenchyma (11). This leads to an increase in stiffness, leaving the tumor more rigid than normal tissues (12).

In the present study, the assessment of the mechanical properties was performed indirectly by measuring the propagation of shear waves within tissue (13). Previous studies – based on finite element simulations as well as experiments using calibrated phantoms – have shown that the presence of micro-obstacles can influence the dispersion relationships of propagating shear waves, and hence alter the apparent mechanical properties of the medium at the macroscopic scale (14). This effect originates from the multiple reflections undergone by the wave as a result of the many collisions with obstacles, leading, overall, to a macroscopic attenuation of the wave (15). Therefore, it is potentially useful to use the apparent macroscopic behavior of the wave in order to sense micro-architectural properties of the medium at the macroscopic scale (16).

Here, we hypothesise that blood vessels represent the main source of wave scattering in the context of MR elastography (MRE). Initial experiments in subcutaneously implanted tumors in mice have demonstrated a close correlation between the mean vessel density and apparent stiffness at the macroscopic scale (17,18). The mean vessel density is often used to quantify therapeutic aspects and is a prognostic indicator in untreated tumor (19–21). The present analysis aims to understand this link between vascular structure and tissue stiffness in more detail. Data are acquired within a well-controlled experiment, removing the confounding effects of cellularity on tissue stiffness (17). We intend to answer the following question: does the propagation and dispersion of shear waves provide information about the presence and structure of the microvasculature? If yes, this would imply that MRE is able to sense the microvascular structure within dispersion properties of shear waves. To verify this hypothesis, an aortic ring model was used. It is based on the

capacity of fragments of rat aorta to spontaneously generate vascular outgrowths in three dimensions once cultured in a bio-matrix gel (22,23). The generated vascular sprouts are composed of the same cell types as *in vivo* blood vessels, making them essentially indistinguishable in their structure, albeit there remains an absence of any vascularization or blood pressure (24–26). As endothelial cells are not altered in culture, they behave like in their *in vivo* environment and constitute vessels of polarized layers of endothelial cells surrounded by pericytes (26). This model is one of the most commonly used methods to study angiogenesis and its mechanisms (27), and is ideal to study the effect of the presence of the blood vessel wall on the dispersion relationship of propagating shear waves.

MATERIALS AND METHODS

Preparation of the vascular outgrowth

The experimental protocol was approved by the local ethics animal care committee (Université Paris Diderot, France). The aortic ring model was designed as described previously (28). Two 11-week-old male Fischer rats (Charles River, L'Arbresle, France) were anesthetized with an intraperitoneal urethane injection (1.01 g/kg; Sigma-Aldrich, St Louis, MO, USA). The abdominal aortas were then excised. Peri-aortic connective tissue, including blood residues, was dissected under optical microscopy, ensuring that the aorta remained wet during the procedure. Following the removal of damaged portions (~2 mm around each edge of the aorta), 18 1-mm-thick aortic rings (hereafter denoted as aortic fragments) were sectioned and washed in cold free minimum essential medium (Sigma-Aldrich). The aortic fragments were then placed in an endothelial cell-specific culture medium, and incubated for 15 h at 37 °C under 5% CO₂ in air. The culture medium was composed of 30 mL of MCDB131 medium supplemented with 25 mM NaHCO₃ (both supplied by Sigma-Aldrich), 20% fetal bovine serum (FBS), 1% L-glutamine and 2% penicillin and streptomycin (last three components supplied by Invitrogen, Carlsbad, CA, USA). Following incubation, three aortic fragments of the 18 prepared fragments were included in 2.5 mL of biomatrix gel (Matrigel 354230; BD Biosciences, San Jose, CA, USA; denoted hereafter as Matrigel) per cell culture insert (Thincert; Greiner bio-one, Kremsmünster, Austria) (29,30). Six inserts were prepared to include the 18 aortic fragments. They were immersed at 37 °C in the same culture medium as above, but here only supplemented with 10% of FBS. The medium was changed every 3 days.

Study design

MRI was performed on the six inserts bearing three aortic fragments each. After 1, 5 and 8 days of culture, two of the six prepared inserts were imaged, providing data from six aortic fragments for each time point. Immediately after the MR scan, optical microscopy was performed to detect the presence and extent of vascular outgrowths in proximity to the aortic fragments.

MR experiments

The inserts were imaged at room temperature (approximately 21 °C) using a horizontal, 7-T, small-animal (16 cm clear bore size with 72 mm free access) Bruker PharmaScan MR scanner

(Erlangen, Germany). An MR planar receive-only surface coil [diameter (\varnothing) = 30 mm] for signal reception was placed around the insert at the level of the Matrigel to maximize the signal-to-noise ratio (Fig. 1A). The radiofrequency coil pre-amplifier was mounted on the custom-built bed and a volume coil (86 mm) was used as excitation coil. The inserts were wrapped in Parafilm® to prevent Matrigel dehydration. The insert temperature was maintained at 37–38 °C via a heating blanket to prevent temperature-dependent changes in shear wave propagation (31). Temperature was monitored in real time with a probe positioned at the surface of the Matrigel. Mechanical vibrations for MRE were induced using a vibrating piston attached to a toothpick passing through the insert membrane (bottom). The piston was connected to an electromagnetic shaker (Brüel & Kjaer, Nærum, Denmark) located outside the MR scanner via a semi-flexible carbon fiber rod. The horizontal vibrations of both the shaker and the rod were converted into vertical vibrations of the piston through a cantilever (Fig. 1B).

The MRI protocol was acquired with the software ParaVision version 5 and consisted of the following.

- (1) Localizer scan. A two-dimensional (2D) fast low-angle shot anatomic tri-axial sequence was applied to localize the aortic fragments. The following imaging parameters were used: TE/TR = 3/100 ms; flip angle, 30°; one average; one repetition; one slice in each direction (axial, coronal, sagittal) with a slice thickness of 2 mm; field of view (FOV), 30 mm × 30 mm; matrix size, 256 × 256; corresponding to a spatial resolution of 117 μ m × 117 μ m; acquisition time, 12 s 800 ms.
- (2) Anatomical scan. 2D T_2 -weighted images were obtained for an accurate depiction of aortic fragments using a rapid acquisition with refocused echoes (RARE) sequence with TE/TR = 11/2000 ms, RARE factor of 8, effective TE of 44 ms, four averages, one repetition, seven contiguous transverse slices with a slice thickness of 0.3 mm, FOV of 29 mm × 29 mm, matrix size of 256 × 256 corresponding to a spatial resolution of 113 μ m × 113 μ m and an acquisition time of 4 min 16 s (Fig. 1A).
- (3) MRE scan. A modified 2D multi-slice spin echo sequence with sinusoidal motion-sensitizing gradients was performed to capture shear wave displacements with a synchronized continuous mechanical excitation for a stationary steady-state wave pattern (13,32). By consecutive application of motion-encoding gradients (300 mT/m) to each gradient axis, the three-dimensional (3D) propagation of the mechanical wave inside the Matrigel was phase encoded over eight time points distributed equally over one vibration period (Fig. 1C). The MRE sequence was applied at five different mechanical

Table 1. TE and TR used for the acquisition of the MR elastography (MRE) scans performed at 100, 115, 125, 135 and 150 Hz with the corresponding acquisition time per direction (acqt/dir)

Frequency (Hz)	TR (ms)	TE (ms)	acqt/dir
150	1080	20	13 min 49 s
135	1044	22	13 min 22 s
125	1016	24	13 min 00 s
115	1043	26	13 min 21 s
100	1060	30	13 min 34 s

frequencies ν from 100 to 150 Hz with one average, seven contiguous transverse slices with a thickness of 0.3 mm positioned at the same location as the seven slices of the anatomical scan, FOV of 29 mm × 29 mm, matrix size of 96 × 96 for a volumetric resolution of 300 μ m × 302 μ m × 302 μ m. TR was held constant between the different frequencies in order to obtain similar relaxation effects among the various acquisitions (Table 1). However, it was necessary to change TE between acquisitions to balance motion sensitivity with data acquisition time, and also to maintain an acceptable duty cycle, which is limited by gradient heating. Variations of TE from 20 to 30 ms had a minimal impact on the signal quality.

MR data processing and analysis

The shear wave speed was calculated in each voxel and for each frequency using custom-developed software. The MRE data were reconstructed using a 3D shear wave inversion algorithm based on a viscoelastic model, assuming isotropic mechanical properties as described in detail previously (Fig. 2B–F) (33,34). In short, first the curl operator was applied to eliminate compressional wave effects. Then, the Helmholtz equation was solved to obtain the complex valued wave vector $k = \beta + i\alpha$. The shear wave speed was then calculated at each voxel via $c_s = (2\pi\nu)/\beta$, where ν is the frequency. The middle three of the seven acquired slices were analysed, and the reported results are an average across these three slices. Data were excluded from the analysis if the average local total wave amplitude at a particular pixel was less than 0.9 μ m over these three slices. This value corresponds to three times the total noise level amplitude (i.e. 0.3 μ m) as established by MRE scans in the absence of any mechanical excitation.

The shear wave speed was calculated by taking the pixel average inside the various regions of interest (ROIs). Nine ROIs were

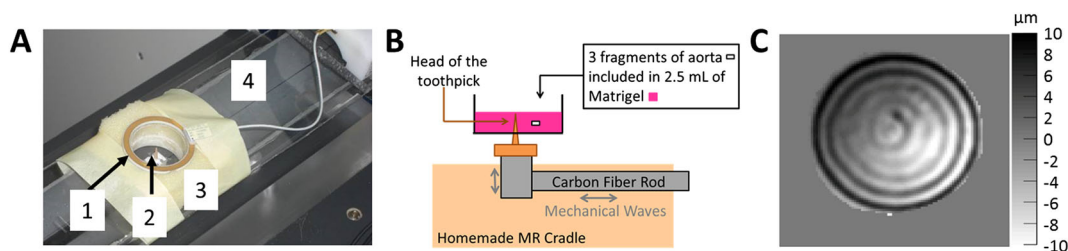


Figure 1. MR elastography (MRE) was performed on rat aortic fragments cultured in Matrigel using a 7-T, small-animal Bruker PharmaScan MR scanner. (A) The experimental set-up for MRE acquisition: 1, 30-mm diameter surface coil; 2, the tip of the toothpick (i.e. the piston); 3, the support to hold the insert; 4, custom-made MR cradle. (B) Schematic representation of the set-up. The horizontal vibration, induced by an electromagnetic shaker (Brüel&Kjaer, Nærum, Denmark) located outside the MR scanner, was converted into vertical vibrations via a cantilever. (C) Images of shear waves within the Matrigel at ν = 150 Hz (μ m).

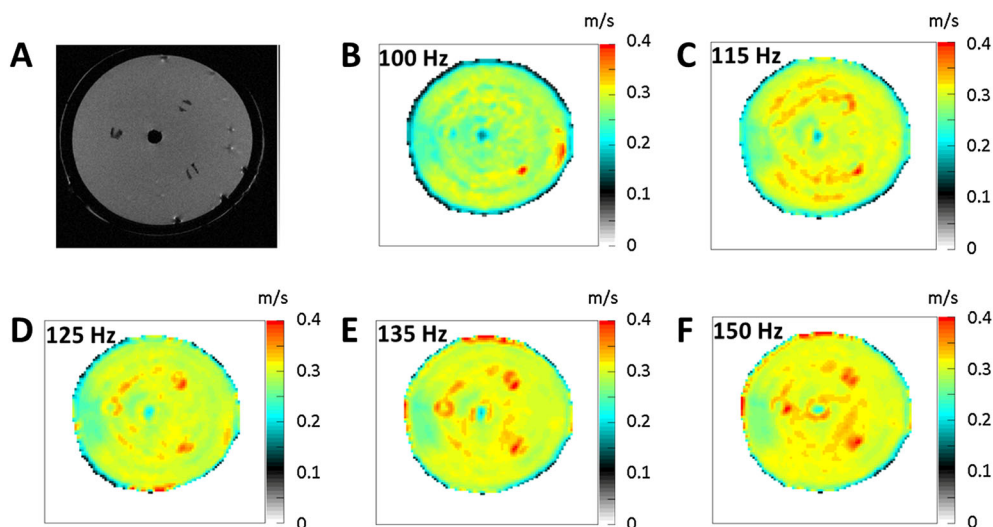


Figure 2. Typical MR images/maps of an insert composed of three aortic fragments cultured in Matrigel. The piston inducing the vibration is located at the center of the insert. (A) High-resolution anatomical T_2 -weighted image. The location of the aortic fragments was highlighted by the hypo-signal of the aortic walls. The presence or absence of microscopic vascular outgrowths could not be determined using MR anatomical images at the chosen spatial resolution ($113 \mu\text{m} \times 113 \mu\text{m}$ in-plane). Air bubbles created during the sample preparation could also be observed as hypo-signal within the Matrigel. (B–F) Shear wave speed maps obtained at mechanical vibration frequencies of 100, 115, 125, 135 and 150 Hz, respectively. The circular ring artefact originates from the shear wave speed reconstruction and not from the aortic fragments, as can also be seen on the shear wave speed maps obtained in a sample of Matrigel that did not contain aortic fragments (not shown). The impact of the artifact on shear wave speed measurements was minimized by embedding aortic fragments at a constant distance from the vibrating center.

manually drawn for each insert: six reference ROIs in the plain Matrigel (excluding aorta, vascular outgrowths and piston areas) and three ROIs within a ring of $\sim 900 \mu\text{m}$ thickness encompassing the three aortic fragments (here denoted as outgrowth ROIs) (Fig. 3). In addition, for each sample, three ROIs were drawn over the aortic fragment regions to verify that the shear wave speed alteration observed in the outgrowth ROIs was not impacted by the proximity of the aortic fragments. This is crucial as the positioning of the outgrowth ROIs could not exclude the two pixels next to the edge of the aortic fragments (32).

All ROIs were drawn on the anatomical images and then transferred to the matched shear wave maps. Peripheral regions were excluded from the ROIs to avoid edge effects. Air bubbles

created during sample preparation and visible on MR anatomical images were excluded from all ROIs. Baseline stiffness values of the Matrigel were obtained by positioning reference ROIs in close proximity to the aortic fragments, as the Matrigel is an inhomogeneous material. Six reference ROIs were used to adequately sample the Matrigel surrounding the samples. The wave amplitude was not considered as a criterion for the positioning of the ROIs as it exceeded our threshold of reliability over the entire sample for each frequency and at each time point (not shown). Shear wave speeds obtained in the outgrowth and aortic fragment ROIs were normalized to the average shear wave speed of the corresponding reference ROIs. This eliminated potential contributions of changing Matrigel mechanical

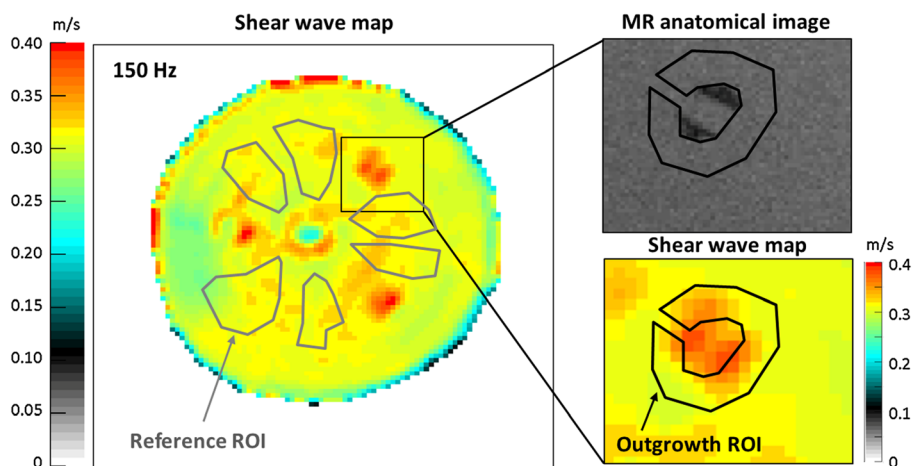


Figure 3. Nine regions of interest (ROIs) were manually drawn for each insert: six reference ROIs in the plain Matrigel (excluding aorta, vascular outgrowths and piston) and three outgrowth ROIs within a ring of $\sim 900 \mu\text{m}$ radius encompassing the three aortic fragments. The drawing of the outgrowth ROIs took into consideration the width of the outgrowth rim visualized by optical microscopy after 8 days of culture and the spatial resolution of the MR anatomical images ($\sim 850 \mu\text{m}$, i.e. approximately seven pixels).

properties with the duration of culture. A separate sample without aortic fragments could not be used for normalization as the ageing process of Matrigel during culture varies from sample to sample because of slight variations in Matrigel composition.

Finally, data were fitted to a frequency power law function according to $c_s \approx \nu^y$, where ν represents the frequency and y the exponent, using GraphPad Prism (version 6.00; La Jolla, CA, USA). The power function is commonly used to represent the frequency-dependent mechanical behavior of viscoelastic soft tissues, because it has been recognized that shear rheology in biological soft tissues follows power law behavior at small strains (35–38).

Optical microscopy

Optical microscopy was performed using an inverse DM IRB Microscope (Leica, Wetzlar, Germany), ORCA-03G high-resolution digital camera (Hamamatsu Photonics K.K., Hamamatsu City, Shizuoka, Japan) and cell[^] software (Olympus, Hamburg, Germany). The widths of the outgrowth rim were estimated from photographs of aortic fragments (magnification, $\times 40$) using ImageJ (version 1.45 s).

Statistical analyses

Results are presented as the mean \pm standard deviation. The effects of the duration of culture for the reference ROIs, outgrowth ROIs and normalized outgrowth and aortic fragment ROIs were examined on: (i) the shear wave speed for each frequency using a Kruskal–Wallis test followed by Dunn's multiple comparisons test; and (ii) the exponent y of the power law frequency evolution using an analysis of variance (ANOVA) with Tukey's multiple comparison test. The normality of the distribution was assessed using the Kolmogorov–Smirnov test with Dallal–Wilkinson–Liliefors p value. Statistical tests were performed with GraphPad Prism (version 6.00) and p values of less than 0.05 were considered to be significant.

RESULTS

Reference ROIs

The mechanical properties of the plain Matrigel evolved through time, hence affecting the measured shear wave speed for all frequencies except 115 Hz (Fig. 4A). In the inserts cultivated for 5 days, the

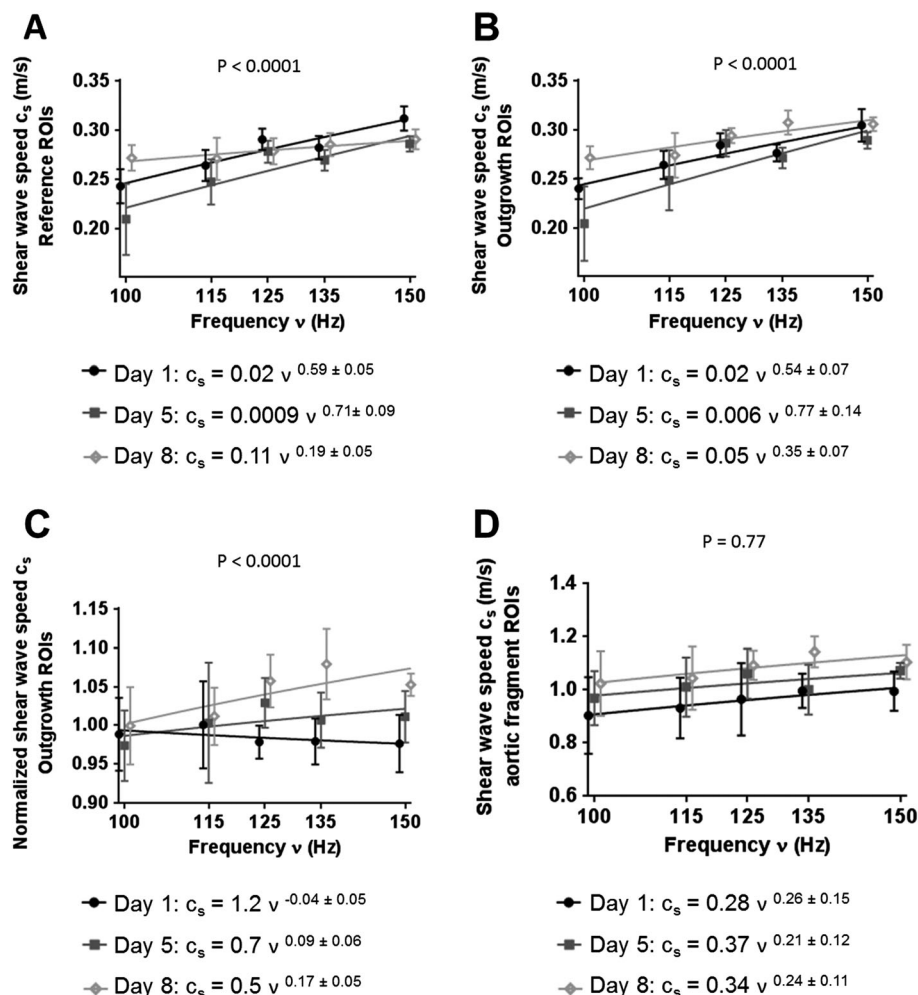


Figure 4. Temporal evolution of the frequency dependence of the shear wave speed measured within the reference regions of interest (ROIs) (A), the outgrowth ROIs (B) and the normalized outgrowth ROIs (C). For each graph, the visibility of the three measurements was improved by slightly shifting them at each frequency. Shear wave speeds (c_s) were fitted to a frequency power law function according to $c_s \approx \nu^y$, where ν is the frequency and y is the exponent. The normalized shear wave speed followed a power law behavior after 5 and 8 days of culture not seen after 1 day of culture. p values of the analysis of variance (ANOVA) test are reported for each graph.

shear wave speed was significantly lower than in those cultivated for 1 day at 150 Hz and for 8 days at 100 and 135 Hz. In addition, in the inserts cultivated for 8 days, the shear wave speed was significantly higher at 100 Hz and significantly lower at 150 Hz than in those cultivated for 1 day (Table 2). In these plain regions, the shear wave speed followed a power law with frequency in all the inserts. However, the duration of culture affected the exponent γ of the frequency dependence, whereby the exponent after 5 days was significantly higher than that after 1 day which was, itself, significantly higher than that after 8 days of culture (Table 3).

Outgrowth ROIs

Similarly, the shear wave speed measured in the regions encompassing the aortic fragments evolved throughout the duration of the experiment at 100, 135 and 150 Hz, but not at 115 and 125 Hz (Fig. 4B). At 100 and 135 Hz, the shear wave speed was significantly higher after 8 days than after 5 days of culture. All other comparisons were non-significant (Table 2).

Similar to the plain Matrigel, in these outgrowth regions, the shear wave speed followed a power law behavior in all the inserts, and the exponent γ was significantly higher in the inserts cultivated for 5 days than after 1 day which was, itself, significantly higher than after 8 days (Table 3).

Normalized outgrowth ROIs

We found that the normalized shear wave speed actually evolved throughout the duration of the experiments at the three highest frequencies, but not at the two lowest frequencies (Fig. 4C). At 125, 135 and 150 Hz, the normalized shear wave speeds were significantly higher in the inserts cultivated for 8 days than in those cultivated for 1 day (Table 2).

The normalized shear wave speed followed a power law behavior only in the inserts cultivated for 5 and 8 days, but not when cultivated for 1 day, with $\gamma = -0.04 \pm 0.05$ compatible with

Table 3. Results of the statistical Tukey's comparisons performed to assess the effect of the duration of culture on exponent γ of the frequency evolution of: (1) the mean shear wave speeds calculated in the reference and outgrowth regions of interest (ROIs); and (2) the mean normalized shear wave speed calculated in the outgrowth and aortic fragment ROIs

Tukey's comparisons		
Reference ROIs	Day 1 <i>versus</i> day 5	$p = 0.02$
	Day 1 <i>versus</i> day 8	$p < 0.0001$
	Day 5 <i>versus</i> day 8	$p < 0.0001$
Outgrowth ROIs	Day 1 <i>versus</i> day 5	$p = 0.004$
	Day 1 <i>versus</i> day 8	$p = 0.01$
	Day 5 <i>versus</i> day 8	$p < 0.0001$
Normalized outgrowth ROIs	Day 1 <i>versus</i> day 5	$p = 0.003$
	Day 1 <i>versus</i> day 8	$p < 0.0001$
	Day 5 <i>versus</i> day 8	$p = 0.06$
Normalized aortic fragment ROIs	Day 1 <i>versus</i> day 5	$p = 0.76$
	Day 1 <i>versus</i> day 8	$p = 0.95$
	Day 5 <i>versus</i> day 8	$p = 0.91$

$\gamma = 0$. The exponents obtained after 5 and 8 days of culture were significantly higher than the exponent obtained after 1 day of culture (Table 3). There was a non-significant trend towards increased exponent ($p = 0.06$) when the culture duration was increased.

Normalized aortic fragment ROIs

The normalized shear wave speed measured in the aortic fragments did not evolve with the duration of culture for the three lowest frequencies (Fig. 4D). However, at 135 Hz, the normalized shear wave speed was significantly higher after 8 days than after

Table 2. Results of the statistical Kruskal–Wallis tests and Dunn's comparisons performed to evaluate the temporal evolution of shear wave speed within the reference regions of interest (ROIs), the outgrowth ROIs and the normalized outgrowth and aortic fragment ROIs for each frequency. After 8 days of culture, the normalized shear wave speed had increased significantly for the three highest frequencies, but not for the two lowest

			Frequency (Hz)				
			100	115	125	135	150
Reference ROIs	Kruskal–Wallis tests		$p < 0.0001$	$p = 0.07$	$p = 0.03$	$p = 0.007$	$p < 0.0001$
		Dunn's comparisons					
		Day 1 <i>versus</i> day 5	$p = 0.24$	$p = 0.45$	$p = 0.05$	$p = 0.08$	$p < 0.0001$
		Day 1 <i>versus</i> day 8	$p = 0.01$	$p > 0.99$	$p = 0.08$	$p > 0.99$	$p = 0.008$
Outgrowth ROIs	Kruskal–Wallis tests		$p < 0.0001$	$p = 0.07$	$p > 0.99$	$p = 0.007$	$p = 0.51$
		Dunn's comparisons					
		Day 1 <i>versus</i> day 5	$p = 0.0004$	$p = 0.31$	$p = 0.22$	$p = 0.001$	$p = 0.04$
		Day 1 <i>versus</i> day 8	$p = 0.70$	$p > 0.99$	$p > 0.99$	$p > 0.99$	$p = 0.14$
Normalized outgrowth ROIs	Kruskal–Wallis tests		$p = 0.09$	$p > 0.99$	$p = 0.35$	$p = 0.05$	$p > 0.99$
		Dunn's comparisons					
		Day 5 <i>versus</i> day 8	$p = 0.002$	$p = 0.35$	$p = 0.39$	$p = 0.005$	$p = 0.08$
		Day 1 <i>versus</i> day 5	$p = 0.63$	$p = 0.87$	$p = 0.0002$	$p = 0.002$	$p = 0.003$
Normalized aortic fragment ROIs	Kruskal–Wallis tests		$p > 0.99$	$p > 0.99$	$p = 0.07$	$p = 0.70$	$p = 0.48$
		Dunn's comparisons					
		Day 1 <i>versus</i> day 5	$p > 0.99$	$p > 0.99$	$p = 0.002$	$p = 0.004$	$p = 0.005$
		Day 1 <i>versus</i> day 8	$p = 0.99$	$p > 0.99$	$p = 0.77$	$p = 0.14$	$p = 0.25$
Normalized aortic fragment ROIs	Kruskal–Wallis tests		$p = 0.40$	$p = 0.30$	$p = 0.24$	$p = 0.003$	$p = 0.004$
		Dunn's comparisons					
		Day 1 <i>versus</i> day 5	$p > 0.99$	$p > 0.91$	$p = 0.58$	$p > 0.99$	$p = 0.12$
		Day 1 <i>versus</i> day 8	$p > 0.48$	$p > 0.34$	$p = 0.31$	$p = 0.01$	$p = 0.009$
Normalized aortic fragment ROIs	Kruskal–Wallis tests		$p = 0.99$	$p > 0.99$	$p > 0.99$	$p = 0.045$	$p > 0.99$
		Dunn's comparisons					
		Day 5 <i>versus</i> day 8	$p = 0.99$	$p > 0.99$	$p > 0.99$	$p = 0.045$	$p > 0.99$

1 or 5 days and, at 150 Hz, it was significantly higher after 8 days than after 1 day of culture (Table 2).

The normalized shear wave speed measured in the aortic fragment regions followed a power law behavior that did not evolve with the duration of culture, as the exponent y remained constant at about 0.2 ($p = 0.77$) (Table 3). This demonstrated that the power law behavior of the shear wave speed observed in the outgrowth ROIs after 5 and 8 days of culture was not caused by the proximity of the aortic fragment, but was a result of the presence of vascular outgrowths.

Optical microscopy observations

No vascular outgrowths were visible after 1 day of culture (Fig. 5A). In the corresponding microscopic images, only macrophages migrating out of the aortic fragments (rounded cells) were evident. The endothelial sprouts typically appeared after 2–3 days of culture and matured with the development of a lumen, and the emergence of pericytes surrounding endothelial cells. After 5 and 8 days of culture, vascular outgrowth rims (approximately 600 μm and 850 μm in radial thicknesses, respectively) were evident around each of the six aortic fragments (Fig. 5B, C).

DISCUSSION

Our results show that the emergence of vascular outgrowths changes the apparent local mechanical properties of the Matrigel, suggesting that the apparent mechanical properties of tissues may be sensitive to changes in microvascular structure. If this holds true *in vivo*, mechanical properties could be useful for the monitoring of vascular changes, such as those occurring in response to anti-angiogenic therapies in cancer.

Imaging biomarkers based on shear wave propagation

In the presence of vascular outgrowths, the normalized shear wave speed increased and followed a frequency power law (not seen in the absence of vascular outgrowths), demonstrating an influence on the dispersion relationship characteristics of propagating shear waves as a result of the presence of the microvasculature. We infer from this that the vascular outgrowths act as micro-obstacles, representing a source for wave scattering that can be sensed by MRE by measurement of the shear wave speed on the macroscopic scale.

The normalization of the shear wave speed measured within the outgrowth ROIs to the reference shear wave speed allowed us to eliminate the contribution of the changes in Matrigel over time. The presence of vascular outgrowths increased the normalized shear

wave speed more prominently at higher than at lower frequencies (Fig. 4C). The difference in sensitivity of the normalized shear wave speed between frequencies may be explained by differences in wavelength. Although a wavelength of 2.0 ± 0.05 mm was measured in Matrigel at 150 Hz, in the same material the wavelength increased to 2.7 ± 0.01 mm at 100 Hz. As a result, lower frequencies and longer wavelengths are less sensitive to microscopic changes in small regions of interest. At 150 Hz, the wavelength was two to three times the width of the vascular outgrowth ROIs (approximately 900 μm), whereas, at 100 Hz, the wavelength was three to four times the width of the outgrowth. Although a choice of a shorter wavelength (i.e. higher frequency) appeared to be relevant here, it was not possible because of the spatial resolution of the MRE acquisition (i.e. 300 μm isotropic). In general, it is recommended that the wavelength covers at least approximately 7–10 pixels to avoid any bias in the shear wave speed calculation as the third spatial derivatives require a minimal support of $5 \times 5 \times 5$ pixels (32). A further increase in frequency, and hence decrease in wavelength, would require increased spatial resolution to meet this criterion and would lead to a prohibitively long acquisition time. A compromise was made between the scan time, the planned resolution of the MR images and the choice of frequencies.

Biological tissue, over a large frequency spectrum, follows power law behavior with the exponent $y \in (0,1)$ (16,36,39,40). The results from this study suggest that this power law behavior can be generated from a branching microvascular structure. Static tests, such as indentation, could find average changes in stiffness, which could arise from differences in the proportions of stiffer vascular components to surrounding tissues (as predicted by mixture theory), but are not as sensitive as MR elastography for the detection of alterations in the arrangement of such structures, as observed in the disordered vascular outgrowth in Matrigel (14).

Two preclinical studies have performed single-frequency MRE on treated tumors, showing a decrease in stiffness when treated, and thus have demonstrated the potential of mechanical properties to become biomarkers of microstructural changes induced by targeted therapies. However, one study associated this softening of the tumor with a decrease in the proliferative cells induced by chemotherapy (41), whereas the other study correlated it with a decrease in mean vessel density induced by a vascular disrupting agent (17). As for anti-angiogenic therapy, the tumor blood vessels are targeted by vascular disrupting agents. Vascular disrupting agents destroy the already established tumor vasculature, resulting in tumor ischemia and necrosis (42,43). Nevertheless, these previous studies have demonstrated that chemical therapies affect the tumor microstructure and coincide with an alteration in the apparent stiffness of the tissue. A relationship

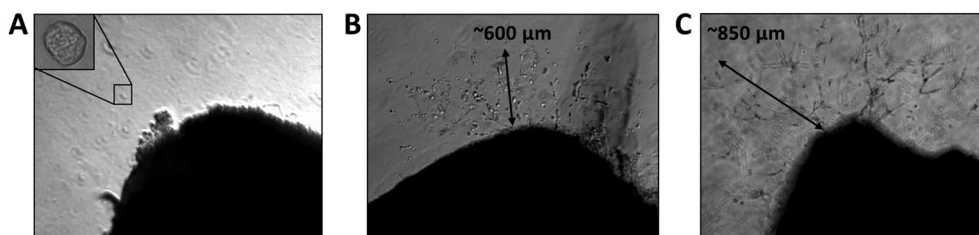


Figure 5. Optical microscopy (magnification, $\times 40$) of aortic fragments after 1 day (A), 5 days (B) and 8 days (C) of culture. No vascular outgrowths were visible around the fragments after 1 day of culture; only macrophages migrating out of the aortic fragment (rounded cells; magnification, $\times 200$) were evident. After 5 days of culture, the rim of outgrowths reached a radius of approximately 600 μm around the aortic fragment and, after 8 days, approximately 850 μm . The blurry appearance of the photograph at day 8 comes from the three-dimensional nature of the vascular outgrowth organization.

between microstructural alterations and softening of the tumor has been suggested, but is difficult to establish because of the complexity of tumor tissue composition. Our findings further support the suggested relationship between microvasculature and tumor stiffness established during spontaneous growth and anti-vascular treatment of a colon tumor model (17). Multifrequency MRE has not yet been used on tumors under targeted therapies, despite its potential for the investigation of the frequency dependence of viscoelastic soft tissues (44–51).

Matrigel

The mechanical properties of plain Matrigel changed with the duration of culture. This is most likely a result of the overall procedure. Two inserts were bathed in the culture medium for 1 day, two for 5 days and two for 8 days. It is likely that the different durations of immersion influenced the mechanical properties of Matrigel. In addition, three vials of 10 ml of Matrigel were used for the preparation of the six inserts. These vials may not have had exactly the same composition and may have contributed to some variability between the mechanical properties of Matrigel.

The mechanical properties measured within the outgrowth ROIs also changed with the duration of culture. These changes were attributed to a combined effect of the vascular outgrowth and the ageing of Matrigel. However, the Matrigel effects appeared to be predominant, as the changes followed a similar pattern to those observed within plain Matrigel. This may be explained by the global composition of the materials in these regions: a large majority of Matrigel with a low density of vascular outgrowths.

Finally, plain Matrigel followed a power law behavior that was attributed to its complex protein mixture.

Limitations

Several limitations have been identified in this study. First, the vascular outgrowths from the aortic ring model were not perfused. Therefore, it may be argued that the mechanical properties in the aortic ring model may differ from those encountered *in vivo*, as it has been reported that endothelial cell stiffness increases in the presence of shear stress (52). Second, only one type of vascular sprout organization was assessed and we did not study how the shear wave dispersion exponent changed with modification of the underlying network of sprouts. Third, the studied frequency bandwidth was limited by the image resolution and sufficient wave penetration within the sample for the highest frequency. Nevertheless, a 50-Hz variation corresponds approximately to that which is clinically feasible. Such a small bandwidth is certainly not sufficient to definitively prove a power law behavior (53). Despite the uncertainties in the rheological description, the presence of vascular outgrowths was capable of altering the apparent shear wave dispersion properties. Fourth, the outgrowth ROIs were relatively small, limiting the size of the analyzed region, and did not permit the exclusion of two pixels next to the edges of the aortic fragments. However, despite this limitation, changes attributed to the presence of vascular outgrowths were observed for the shear wave speed, and this study may represent a starting point for further investigations.

CONCLUSIONS

This study demonstrates that mechanical properties have the potential to become imaging biomarkers to 'sense' microvasculature

changes, as the blood vessel walls induce shear wave dispersion that can be probed by MRE. This was shown by the alteration in the apparent mechanical properties of a biomatrix as a result of the emergence of vascular outgrowths from a ring aortic model. However, an understanding of the effect of micro-obstacles on wave propagation is essential to extract microstructural information on biological tissues from the apparent macroscopic mechanical properties as measured by MRE. This relationship is currently under investigation.

Acknowledgements

The authors thank the staff at Fédération de Recherche en Imagerie Multimodalité (FRIM) MRI facility (Institute Claude Bernard, Paris, France). The authors acknowledge financial support from the National Institute for Health Research (NIHR) Biomedical Research Centre based at Guy's and St Thomas' NHS Foundation Trust and King's College London. The views expressed are those of the author(s) and not necessarily those of the NHS, the NIHR or the Department of Health. This project was funded by the French National Cancer Institute (INCA).

REFERENCES

1. Nakamura H, Ito N, Kotake F, Mizokami Y, Matsuoka T. Tumor-detecting capacity and clinical usefulness of SPIO-MRI in patients with hepatocellular carcinoma. *J. Gastroenterol.* 2000; 35(11): 849–855.
2. Harisinghani MG, Jhaveri KS, Weissleder R, Schima W, Saini S, Hahn PF, Mueller PR. MRI contrast agents for evaluating focal hepatic lesions. *Clin. Radiol.* 2001; 56(9): 714–725.
3. Caravan P, Ellison JJ, McMurry TJ, Laufer RB. Gadolinium(III) chelates as MRI contrast agents: structure, dynamics, and applications. *Chem. Rev.* 1999; 99(9): 2293–2352.
4. Eisenhauer EA, Therasse P, Bogaerts J, Schwartz LH, Sargent D, Ford R, Dancey J, Arbuck S, Gwyther S, Mooney M, Rubinstein L, Shankarg L, Doddg L, Kaplanj R, Lacombe D, Verweijk J. New response evaluation criteria in solid tumours: revised RECIST guideline (version 1.1). *Eur. J. Cancer* 2009; 45(2): 228–247.
5. European Association for the Study of the Liver, European Organisation for Research and Treatment of Cancer EASL-EORTC clinical practice guidelines: management of hepatocellular carcinoma. *J. Hepatol.* 2012; 56(4): 908–943.
6. Lencioni R, Llovet JM. Modified RECIST (mRECIST) assessment for hepatocellular carcinoma. *Semin. Liver Dis.* 2010; 30(1): 52–60.
7. Edeline J, Boucher E, Rolland Y, Vauleon E, Pracht M, Perrin C, Le Roux C, Raoul JL. Comparison of tumor response by Response Evaluation Criteria in Solid Tumors (RECIST) and modified RECIST in patients treated with sorafenib for hepatocellular carcinoma. *Cancer* 2012; 118(1): 147–156.
8. James K, Eisenhauer E, Christian M, Terenziani M, Vena D, Muldal A, Therasse P. Measuring response in solid tumors: unidimensional versus bidimensional measurement. *J. Natl. Cancer Inst.* 1999; 91(6): 523–528.
9. Bronchud MH, Foote M, Giaccone G, Olopade O, Workman P (eds). *Principles of Molecular Oncology*. Humana Press: Totowa, NJ, USA, 2008.
10. Fung YC (ed). *Biomechanics, Mechanical Properties of Living Tissues*, 2nd edn. Springer-Verlag: New York, USA, 1993.
11. Sanz-Cameno P, Trapero-Marugan M, Chaparro M, Jones EA, Moreno-Otero R. Angiogenesis: from chronic liver inflammation to hepatocellular carcinoma. *J. Oncol.* 2010; 2010: 272170.
12. Garteiser P, Doblas S, Daire JL, Wagner M, Leitao H, Vilgrain V, Sinkus R, Van Beers BE. MR elastography of liver tumours: value of viscoelastic properties for tumour characterisation. *Eur. Radiol.* 2012; 22(10): 2169–2177.
13. Muthupillai R, Lomas DJ, Rossman PJ, Greenleaf JF, Manduca A, Ehman RL. Magnetic resonance elastography by direct visualization of propagating acoustic strain waves. *Science* 1995; 269(5232): 1854–1857.
14. Lambert SA, Näsholm SP, Nordsletten D, Michler C, Juge L, Bilston LE, Guzina B, Holm S, Sinkus R. Bridging three orders of magnitude: multiple scattered waves sense fractal microscopic structures via dispersion. *Phys. Rev. Lett.* 2015; 115: 094301.
15. O'Doherty RF, Anstey NA. Reflections on amplitudes. *Geophys. Prospect.* 1971; 19(3): 430–458.

16. Holm S, Sinkus R. A unifying fractional wave equation for compressional and shear waves. *J. Acoust. Soc. Am.* 2010; 127(1): 542–559.
17. Juge L, Doan BT, Seguin J, Albuquerque M, Larrat B, Mignet N, Chabot GG, Scherman D, Paradis V, Vilgrain V, Van Beers BE, Sinkus R. Colon tumor growth and antivasular treatment in mice: complementary assessment with MR elastography and diffusion-weighted MR imaging. *Radiology* 2012; 264(2): 436–444.
18. Jamin Y, Boulton JK, Li J, Popov S, Garteiser P, Ulloa JL, Cummings C, Box G, Eccles SA, Jones C, Waterton JC, Bamber JC, Sinkus R, Robinson SP. Exploring the biomechanical properties of brain malignancies and their pathologic determinants in vivo with magnetic resonance elastography. *Cancer Res.* 2015 Apr 1;75(7): 1216–1224.
19. Weidner N, Semple JP, Welch WR, Folkman J. Tumor angiogenesis and metastasis—correlation in invasive breast carcinoma. *N. Engl. J. Med.* 1991; 324(1): 1–8.
20. Weidner N, Folkman J, Pozza F, Bevilacqua P, Allred EN, Moore DH, Meli S, Gasparini G. Tumor angiogenesis: a new significant and independent prognostic indicator in early-stage breast carcinoma. *J. Natl. Cancer Inst.* 1992; 84(24): 1875–1887.
21. Weidner N, Carroll PR, Flax J, Blumenfeld W, Folkman J. Tumor angiogenesis correlates with metastasis in invasive prostate carcinoma. *Am. J. Pathol.* 1993; 143(2): 401–409.
22. Aplin AC, Fogel E, Zorzi P, Nicosia RF. The aortic ring model of angiogenesis. *Methods Enzymol.* 2008; 443: 119–136.
23. Nicosia RF. The aortic ring model of angiogenesis: a quarter century of search and discovery. *J. Cell. Mol. Med.* 2009; 13(10): 4113–4136.
24. Kawasaki S, Mori M, Arai M. Capillary growth of rat aortic segments cultured in collagen gel without serum. *Acta Pathol. Jpn.* 1989; 39(11): 712–718.
25. Nicosia RF, Bonanno E, Villaschi S. Large-vessel endothelium switches to a microvascular phenotype during angiogenesis in collagen gel culture of rat aorta. *Atherosclerosis* 1992; 95(2–3): 191–199.
26. Nicosia RF, Villaschi S. Rat aortic smooth muscle cells become pericytes during angiogenesis in vitro. *Lab. Invest.* 1995; 73(5): 658–666.
27. Go RS, Owen WG. The rat aortic ring assay for in vitro study of angiogenesis. *Methods Mol. Med.* 2003; 85: 59–64.
28. Nicosia RF, Ottinetti A. Growth of microvessels in serum-free matrix culture of rat aorta. A quantitative assay of angiogenesis in vitro. *Lab. Invest.* 1990; 63(1): 115–122.
29. Hughes CS, Postovit LM, Lajoie GA. Matrigel: a complex protein mixture required for optimal growth of cell culture. *Proteomics* 2010; 10(9): 1886–1890.
30. Nicosia RF, Ottinetti A. Modulation of microvascular growth and morphogenesis by reconstituted basement membrane gel in three-dimensional cultures of rat aorta: a comparative study of angiogenesis in matrigel, collagen, fibrin, and plasma clot. *In Vitro Cell. Dev. Biol.* 1990; 26(2): 119–128.
31. Soofi SS, Last JA, Liliensiek SJ, Nealey PF, Murphy CJ. The elastic modulus of Matrigel as determined by atomic force microscopy. *J. Struct. Biol.* 2009; 167(3): 216–219.
32. Sinkus R, Tanter M, Xydeas T, Catheline S, Bercoff J, Fink M. Viscoelastic shear properties of in vivo breast lesions measured by MR elastography. *Magn. Reson. Imaging* 2005; 23(2): 159–165.
33. Sinkus R, Siegmann K, Xydeas T, Tanter M, Claussen C, Fink M. MR elastography of breast lesions: understanding the solid/liquid duality can improve the specificity of contrast-enhanced MR mammography. *Magn. Reson. Med.* 2007; 58(6): 1135–1144.
34. Green MA, Bilston LE, Sinkus R. In vivo brain viscoelastic properties measured by magnetic resonance elastography. *NMR Biomed.* 2008; 21(7): 755–764.
35. Liu Z, Bilston L. On the viscoelastic character of liver tissue: experiments and modelling of the linear behaviour. *Biorheology* 2000; 37(3): 191–201.
36. Szabo T. Time domain wave equations for lossy media obeying a frequency power law. *J. Acoust. Soc. Am.* 1994; 96: 491–500.
37. Guo J, Posnansky O, Hirsch S, Scheel M, Taupitz M, Braun J, Sack I. Fractal network dimension and viscoelastic powerlaw behavior: II. An experimental study of structure-mimicking phantoms by magnetic resonance elastography. *Phys. Med. Biol.* 2012; 57(12): 4041–4053.
38. Posnansky O, Guo J, Hirsch S, Papazoglou S, Braun J, Sack I. Fractal network dimension and viscoelastic powerlaw behavior: I. A modeling approach based on a coarse-graining procedure combined with shear oscillatory rheometry. *Phys. Med. Biol.* 2012; 57(12): 4023–4040.
39. Bagley RL, Torvik PJ. A theoretical basis for the application of fractional calculus to viscoelasticity. *J. Rheol.* 1983; 27: 201.
40. Clausen A, Shalizi CR, Newman MEJ. Power-law distributions in empirical data. *Siam. Rev.* 2009; 51(4): 661–703.
41. Pepin KM, Chen J, Glaser KJ, Mariappan YK, Reuland B, Ziesmer S, Carter R, Ansell SM, Ehman RL, McGee KP. MR elastography derived shear stiffness—a new imaging biomarker for the assessment of early tumor response to chemotherapy. *Magn. Reson. Med.* 2014; 71(5): 1834–1840.
42. Gridelli C, Rossi A, Maione P, Rossi E, Castaldo V, Sacco PC, Colantuoni G. Vascular disrupting agents: a novel mechanism of action in the battle against non-small cell lung cancer. *Oncologist* 2009; 14(6): 612–620.
43. Siemann DW, Bibby MC, Dark GG, Dicker AP, Eskens FA, Horsman MR, Marme D, Lorusso PM. Differentiation and definition of vascular-targeted therapies. *Clin. Cancer Res.* 2005; 11(2 Pt 1): 416–420.
44. Wuerfel J, Paul F, Beierbach B, Hamhaber U, Klatt D, Papazoglou S, Zipp F, Martus P, Braun J, Sack I. MR-elastography reveals degradation of tissue integrity in multiple sclerosis. *Neuroimage* 2010; 49(3): 2520–2525.
45. Klatt D, Hamhaber U, Asbach P, Braun J, Sack I. Noninvasive assessment of the rheological behavior of human organs using multifrequency MR elastography: a study of brain and liver viscoelasticity. *Phys. Med. Biol.* 2007; 52(24): 7281–7294.
46. Asbach P, Klatt D, Hamhaber U, Braun J, Somasundaram R, Hamm B, Sack I. Assessment of liver viscoelasticity using multifrequency MR elastography. *Magn. Reson. Med.* 2008; 60(2): 373–379.
47. Feng Y, Clayton EH, Chang Y, Okamoto RJ, Bayly PV. Viscoelastic properties of the ferret brain measured in vivo at multiple frequencies by magnetic resonance elastography. *J. Biomech.* 2013; 46(5): 863–870.
48. Clayton EH, Garbow JR, Bayly PV. Frequency-dependent viscoelastic parameters of mouse brain tissue estimated by MR elastography. *Phys. Med. Biol.* 2011; 56(8): 2391–2406.
49. Debernard L, Robert L, Charleux F, Bensamoun SF. A possible clinical tool to depict muscle elasticity mapping using magnetic resonance elastography. *Muscle Nerve* 2013; 47(6): 903–908.
50. Ronot M, Lambert SA, Wagner M, Garteiser P, Doblas S, Albuquerque M, Paradis V, Vilgrain V, Sinkus R, Van Beers BE. Viscoelastic parameters for quantifying liver fibrosis: three-dimensional multifrequency MR elastography study on thin liver rat slices. *PLoS One* 2014; 9(4): e94679.
51. Ronot M, Lambert S, Elrief L, Doblas S, Rautou PE, Castera L, Vilgrain V, Sinkus R, Van Beers BE, Garteiser P. Assessment of portal hypertension and high-risk oesophageal varices with liver and spleen three-dimensional multifrequency MR elastography in liver cirrhosis. *Eur. Radiol.* 2014; 24(6): 1394–1402.
52. Sato M, Levesque MJ, Nerem RM. Micropipette aspiration of cultured bovine aortic endothelial cells exposed to shear stress. *Arteriosclerosis* 1987; 7(3): 276–286.
53. Fabry B, Maksym GN, Butler JP, Glogauer M, Navajas D, Taback NA, Millet EJ, Fredberg JJ. Time scale and other invariants of integrative mechanical behavior in living cells. *Phys. Rev. E Stat. Nonlin. Soft Matter Phys.* 2003; 68(4 Pt 1): 041914.